

# SUPPLEMENTARY MATERIAL: Magnetic instabilities in doped $\text{Fe}_2YZ$ full-Heusler thermoelectric compounds

Sébastien Lemal,<sup>1</sup> Fabio Ricci,<sup>1</sup> Daniel I. Bilec,<sup>2</sup> Matthieu J. Verstraete,<sup>1,3</sup> and Philippe Ghosez<sup>1</sup>

<sup>1</sup>*Physique Théorique des Matériaux, Q-MAT, CESAM,  
Université de Liège (B5), B-4000 Liège, Belgium*

<sup>2</sup>*Faculty of Physics, Babeş-Bolyai University, 1 Kogălniceanu, 400084 Cluj-Napoca, Romania*

<sup>3</sup>*European Theoretical Spectroscopy Facility, <http://www.etsf.eu/>*

(Dated: October 3, 2019)

## Motivations

The main purpose of the  $n$ -type doped  $\text{Fe}_2YZ_{1-x}A_x$  ( $\text{Fe}_2YZ_A$ ) compounds is to have the  $A$  impurities acting as shallow donors so that they do not perturb the states close to the band gap keeping thus other properties of the pristine compounds unaffected. The shift of the chemical potential on the Fe  $e_g$  band is done by substituting part of the  $Z$  atoms with  $A$  atoms so that the atomic number goes from  $Z_A = Z_Z + 1$ . Hence, the substitutional atom is similar to the  $Z$  atom in term of size, mass and electronic structure just with one additional electron. In these conditions, we observe whether the Fermi level ( $E_F$ ) is shifted at the maximum of the spectral power factor [1].

## Technical details

DFT calculations were performed with the CRYSTAL code [2, 3]. The B1 Wu-Cohen [4] (B1-WC) hybrid functional has been used for all calculations. Doping was modelled by the means of cubic and tetragonal supercells, giving a range of doping from  $3.8 \times 10^{20} \text{ cm}^{-3}$  to  $1.5 \times 10^{21} \text{ cm}^{-3}$ , falling into the range of doping needed to maximize the power factor as identified in Ref. 1. The following compounds are studied:  $\text{Fe}_2\text{TiSn}_{\text{Sb}}$ ,  $\text{Fe}_2\text{TiSiP}$ ,  $\text{Fe}_2\text{VAl}_{\text{Si}}$ ,  $\text{Fe}_2\text{TaGa}_{\text{Ge}}$  and  $\text{Fe}_2\text{NbGa}_{\text{Ge}}$ . In all cases, the compositions  $x = 0, 1/32$  and  $1/16$  have been considered. For the specific case of  $\text{Fe}_2\text{TiSn}_{\text{Sb}}$ , we also investigated the doping value  $x = 1/48$  with a  $2 \times 2 \times 3$  supercell.

The basis set used are taken from Ref. 5 for Fe, Ref. 6 for Ti, Ref. 7 for Sn, Sb, Nb, Al and Ta, Ref. 8 for V and Ge, Ref. 9 for Ga, and Ref. 10 for Si. Spin-polarization is considered: an initial magnetic moment of  $1 \mu_B/\text{u.c.}$  is imposed to the unit cell during the first 3 steps of the self-consistent cycle. Different Monkhorst-Pack [11] meshes of  $k$ -points were used: i) a  $9 \times 9 \times 9$  mesh was used for the structural relaxation of the undoped unit cells; ii) a  $5 \times 5 \times 5$  mesh was used for the structural relaxation of the doped supercells; iii) a  $10 \times 10 \times 10$  mesh was used for the computation of the electronic properties; and iv) a  $32 \times 32 \times 32$  mesh was used for the computation of the thermoelectric properties after interpolation. The energy convergence criterion was fixed to  $10^{-9}$  Ha. For

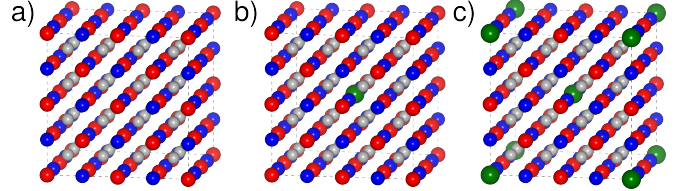


FIG. 1. Structure of  $\text{Fe}_2YZ$  compounds with, from left to right, no impurity, one impurity and two impurities (green) in the  $2 \times 2 \times 2$  supercell.

relaxation, we fixed a threshold of  $3 \times 10^{-4}$  Ha/Bohr on the root-mean square values of energy gradients and of  $1.2 \times 10^{-3}$  Bohr on the root-mean square values of atomic displacements. A temperature smearing of the Fermi surface was set to  $3.2 \times 10^{-4}$  Ha. For transport properties, the BoltzTraP [12] code was used, which performs calculation within the constant relaxation time approximation (CRTA). The constant relaxation time  $\tau = 3.4 \times 10^{-14}$  s is taken from Ref. 1. Further information on its estimation is given in the Supplementary Materials of Ref. 1.

The DFT+ $U$  simulations using the ABINIT code [13] were performed within the PBE [14] flavour of the generalized gradient approximation (GGA). We make use of the  $U$  correction in order to treat the electronic correlations on the transition metal atoms  $d$  orbitals [15] and we self-consistently determined the Hubbard-like  $U$  correction using the linear response formalism [16], with  $5.0 \times 10^{-2}$  eV degree of convergence on the  $U$  values, corresponding to a the lattice parameter optimization tolerance of the order of  $10^{-3}$  Å. We used projected augmented-wave (PAW) pseudopotentials [17] taken from the JTH table [18] and in order to achieve a satisfactory degree of convergence ( $\sim 0.01$  meV energy differences) the plane wave expansion has been truncated at a cutoff energy of 653 eV and the integrations over the Brillouin Zone were performed considering  $20 \times 20 \times 20$  uniform Monkhorst and Pack grid [11].

In this framework, we obtain (i) lattice parameters in perfect agreement with available experiments ( $\Delta a < 5 \%$ , see Tab. I); (ii) similar static and dynamic charges on each atomic site with respect to B1-WC calculations (not shown) and (iii) band structures reasonably similar to B1-WC (similar band gaps, and states at the valence

$\text{Fe}_2YZ$	$U_{\text{Fe}}$ (eV)	$U_Y$ (eV)	$E_g$ (eV)	$a$ (Å)	$a_{\text{EXP}}$ (Å)	Ref.
$\text{Fe}_2\text{TiSn}$	5.09	2.62	1.29	6.069	6.074	[19]
$\text{Fe}_2\text{TiSi}$	5.02	2.47	1.41	5.714	5.720	[20]
$\text{Fe}_2\text{VAl}$	5.02	4.86	1.09	5.733	5.761	[21]
$\text{Fe}_2\text{TaGa}$	5.02	1.28	1.35	5.929	-	-
$\text{Fe}_2\text{NbGa}$	5.03	1.55	1.02	5.934	-	-
$X_2YZ$	$U_X$ (eV)	$U_Y$ (eV)	$E_g$ (eV)	$a$ (Å)	$a_{\text{EXP}}$ (Å)	Ref.
$\text{Ru}_2\text{ZrSn}$	2.90	1.09	0.17	6.479	-	-
+ SOC	2.88	1.03	0.15	6.479	-	-
$\text{Os}_2\text{HfSn}$	2.67	0.99	0.59	6.484	-	-
+ SOC	2.82	0.25	0.14	6.483	-	-

TABLE I. GGA+ $U$  study: self-consistently determined  $U$  for the transition metal atoms (Fe and  $Y$  sites) in the overall compounds; obtained energy gap ( $E_g$ ) and related optimized and experimentally available lattice parameters  $a$ .

and conduction edges, see Fig. 2). It is worth noticing however that, just for  $\text{Fe}_2\text{TiSn}$  and similarly for  $\text{Fe}_2\text{TiSi}$  (not shown), using the self-consistent  $U_{\text{Ti}}$  results in a Ti  $e_g$  (dispersive) band, too low in energy, with a minimum touching the Fe  $e_g$  (flat) band. As illustrated in Fig. 3, using a larger  $U_{\text{Ti}} = 5.60$  eV permits to recover a better agreement in the bottom of the conduction band, yielding thermoelectric properties similar to those determined from the B1-WC band structure.

In addition, the effect of the spin-orbit coupling (SOC) has been checked on the  $4d$  and  $5d$  transition metals computing again the self-consistent  $U$  values, the equilibrium lattice parameters and the electronic properties. The results are reported on Tab. I and the band structure differences are shown in Fig. 4, 5, 6, 7, 8, 9 and 10.

### Non-magnetic shallow donor levels

As we have seen in the main text (Fig. 1(b)), the mechanism driving the doping consequences in the non-magnetic constrained phase is shallow donor-like. A further proof for this behaviour can be given exploiting the Effective Mass Theory [22–24]. In this approach, the binding energy of the donor level  $E_D^b$  with respect to the conduction band minimum (CBM) and the spatial extension  $a_D$  of the related wave function can be expressed as:

$$E_D^b = \frac{m^*}{m} \frac{hc R_\infty}{\varepsilon_\infty^2} \quad (1)$$

$$a_D = \frac{m}{m^*} \varepsilon_\infty a_B \quad (2)$$

where  $m$  ( $m^*$ ) is the mass (effective mass) of the additional electron,  $\varepsilon_\infty = 25.55$  is the crystal dielectric constant (estimated within GGA+ $U$ ),  $R_\infty$  is the Rydberg constant with  $hc R_\infty = 13.61$  eV and  $a_B = 0.53$  Å, the Bohr radius. In the case of  $\text{Fe}_2\text{TiSn}$ , the effective masses

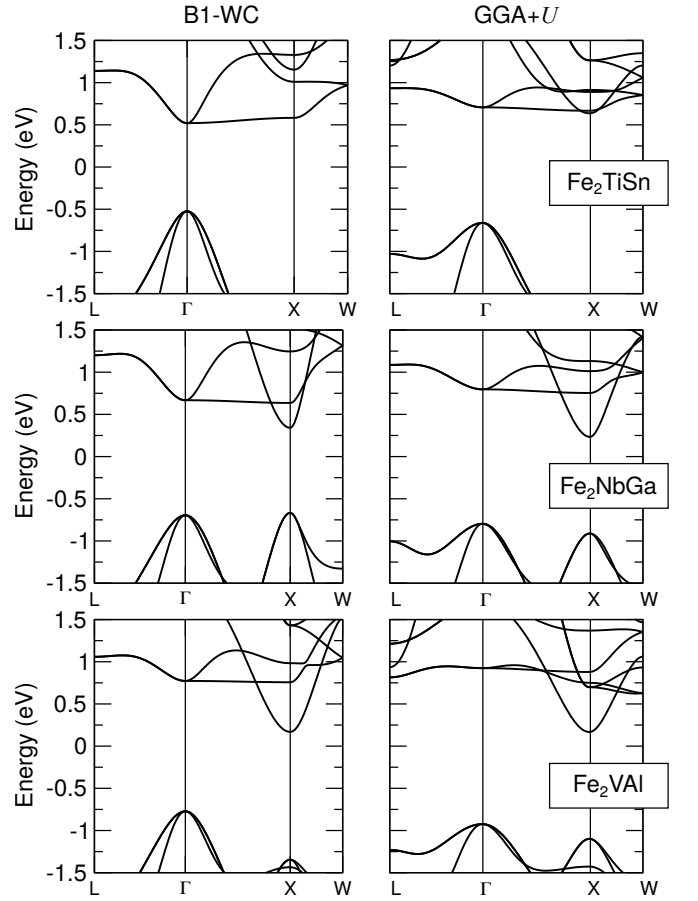


FIG. 2. Band structures of  $\text{Fe}_2\text{TiSn}$ ,  $\text{Fe}_2\text{NbGa}$  and  $\text{Fe}_2\text{VAl}$  as calculated from B1-WC and GGA+ $U$  with self-consistent  $U$ 's.

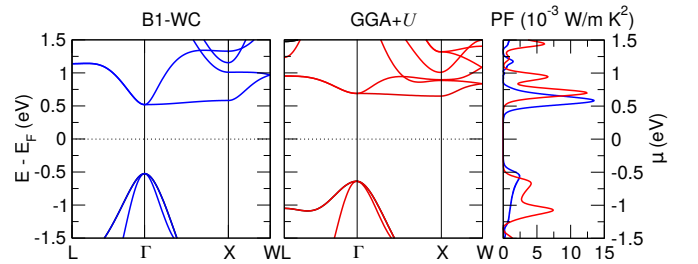


FIG. 3. Band structures of  $\text{Fe}_2\text{TiSn}$  as calculated from B1-WC and GGA+ $U$  ( $U_{\text{Fe}} = 5.09$  eV,  $U_{\text{Ti}} = 5.60$  eV). The spectral power factors as calculated from both band structures, in the rigid band approximation, are shown on the right. Both methods reproduces the peak arising from the Fe  $e_g$  band at the CBM.

related to the dispersive ( $m_l$ ) and flat ( $m_h$ ) bands, were estimated by Bilc and coworkers [1] to be  $m_l = 0.3 m$  and  $m_h = 26 m$ . The two separated contributions give:

$$E_D^b(m_l) \approx 4.6 \text{ meV} \text{ and } a_D(m_l) \approx 45.0 \text{ Å} ; \quad (3)$$

$$E_D^b(m_h) \approx 540.0 \text{ meV} \text{ and } a_D(m_h) \approx 0.5 \text{ Å} . \quad (4)$$

It is clear at this point that the results in Eq. (3) are in agreement with the picture given for Fig. 1(b) where the

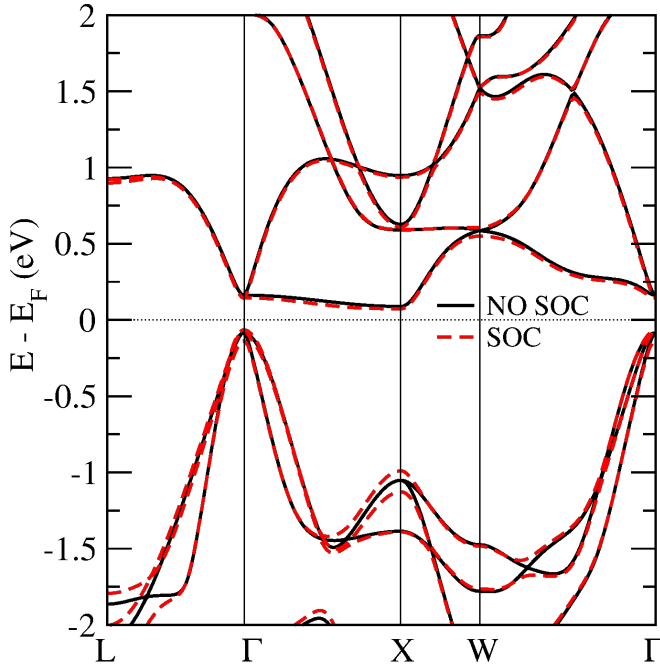


FIG. 4.  $\text{Ru}_2\text{ZrSn}$  band structures accounting for or not the SOC interaction, as calculated from GGA+ $U$ .

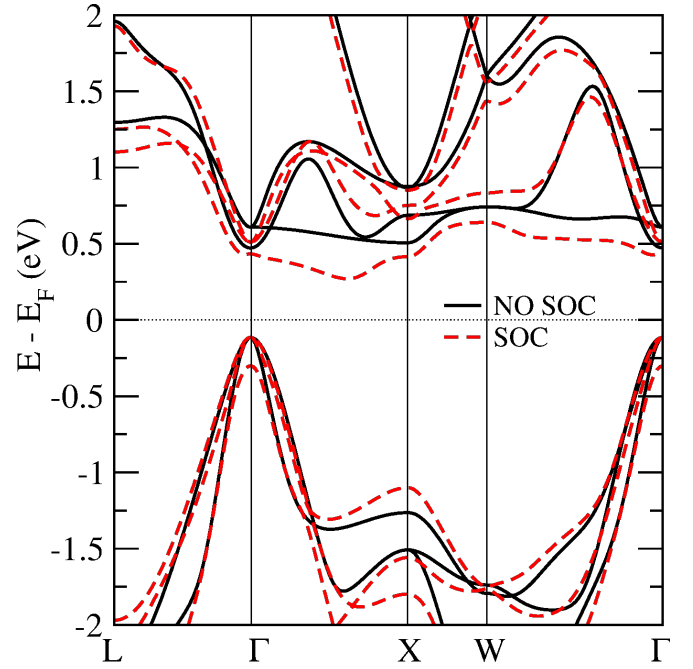


FIG. 6.  $\text{Os}_2\text{HfSn}$  band structures accounting for or not the SOC interaction, as calculated from GGA+ $U$ .

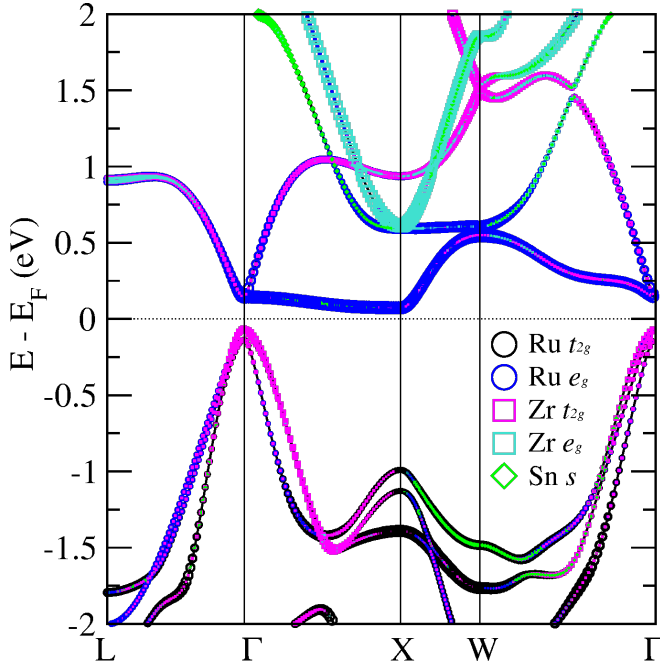


FIG. 5.  $\text{Ru}_2\text{ZrSn}$  orbital-weighted band structures including SOC interaction, as calculated from GGA+ $U$ .

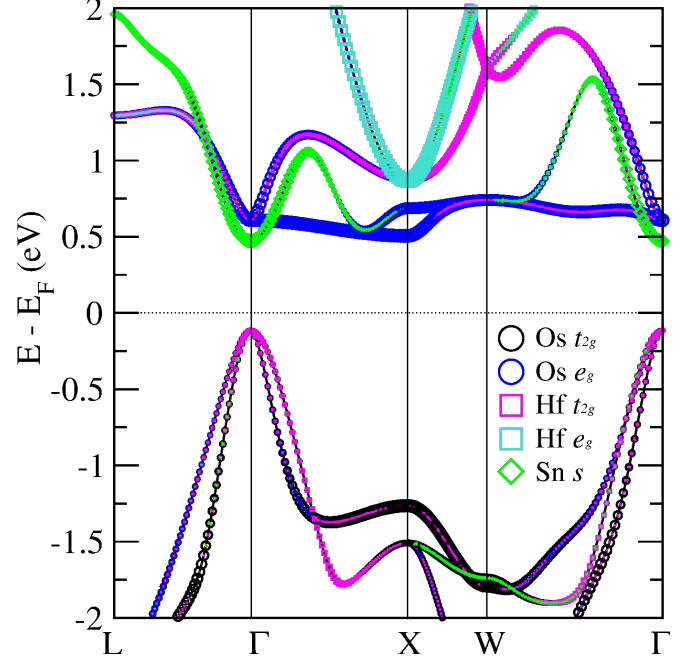


FIG. 7.  $\text{Os}_2\text{HfSn}$  orbital-weighted band structures without SOC interaction, as calculated from GGA+ $U$ .

shallow donor mechanism induces a doping level practically incorporated to the CBM and causing a rigid-band-like shift of the chemical potential. On the contrary, in case of flat bands the doping level would be completely isolated and far from the CBM, as quantified by Eq. (4). However, as explained in the main text, the electronic localization is driven by the exchange interaction and not

by the (shallow donor) nature of doping.

### Magnetic phases in doped compounds

The magnetization energies  $\Delta E$  of the doped  $\text{Fe}_2\text{YZ}_A$  phases (difference between NM and FM total energies)

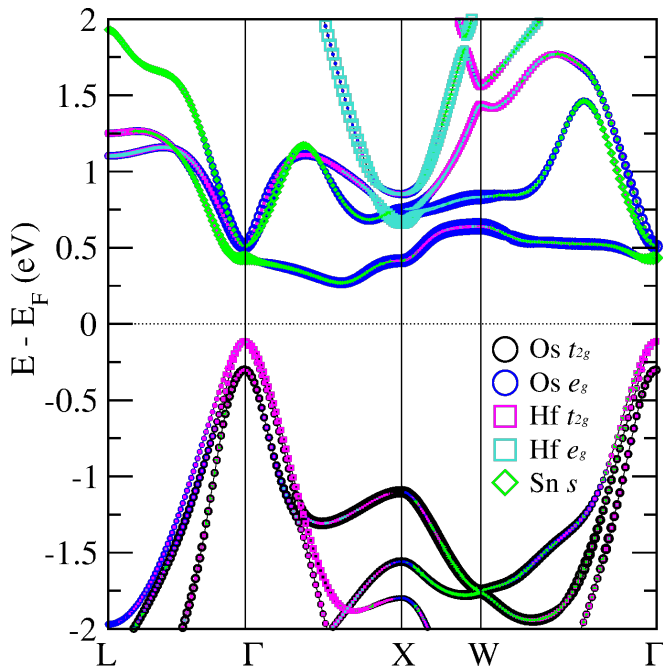


FIG. 8.  $\text{Os}_2\text{HfSn}$  orbital-weighted band structures including SOC interaction, as calculated from GGA+ $U$ .

are given in Table II. From here, it is evident the stability of the FM phase for  $\text{Fe}_2\text{TiSn}_{\text{Sb}}$ ,  $\text{Fe}_2\text{TiSiP}$  and  $\text{Fe}_2\text{TaGa}_{\text{Ge}}$ . Concerning the  $\text{Fe}_2\text{VAl}_{\text{Si}}$ , no magnetic phase can be stabilized while for  $\text{Fe}_2\text{NbGa}_{\text{Ge}}$  the NM phase is the groundstate.

In addition to the FM phase, different antiferromagnetic (AFM) configurations have been explored with both B1-WC and GGA+ $U$  methods. However, for each one of these the charge density cannot be converged, hence no related results can be shown at present. This behaviour, nevertheless, suggests that the FM phase is robust, as expected from the large exchange-splittings found in the band structures. We also stress that the density of dopants (fixed by the choice of the supercell sizes) guaranties that the carriers density satisfies the Stoner criterion for itinerant-electron magnetism.

### Charge localization in doped systems

The strong donor charge density surrounding the defect that typically accompanies the ferromagnetic (FM) phase transition can be seen from the charge density projected on the occupied conduction states (Fig. 11). This behaviour is the consequence of the highly localized nature of the Fe  $e_g$  orbitals accommodating the additional electrons. In the case of  $\text{Fe}_2\text{TiSn}_{\text{Sb}}$  (similar to  $\text{Fe}_2\text{TiSiP}$  due to the similar band structure, see main text), the shape of the projected electron density corresponds exactly to the magnetization density, with the whole form of  $e_g$  orbital near the Sb impurity. In the case

$\text{Fe}_2\text{YZ}_A$	$x$	$\Delta E$ (meV)
$\text{Fe}_2\text{TiSn}_{\text{Sb}}$	1/32	75
	1/16	166
$\text{Fe}_2\text{TiSiP}$	1/32	51
	1/16	105
$\text{Fe}_2\text{VAl}_{\text{Si}}$	1/32	0
	1/16	0
$\text{Fe}_2\text{TaGa}_{\text{Ge}}$	1/32	37
	1/16	98
$\text{Fe}_2\text{NbGa}_{\text{Ge}}$	1/32	-34
	1/16	-7

TABLE II. Magnetization energies ( $\Delta E = E_{\text{NM}} - E_{\text{FM}}$ ) of the 128-atoms supercells of the doped  $\text{Fe}_2\text{YZ}_A$  at different compositions, as calculated from B1-WC: a positive value indicates that the FM phase is more stable than the NM phase.

of  $\text{Fe}_2\text{NbGa}_{\text{Ge}}$ , the additional charge is fully delocalized over the Fe and Nb atoms with a smaller filling. In the case of  $\text{Fe}_2\text{VAl}_{\text{Si}}$ , the charge delocalizes all over the V atoms as expected from the band structure (see Fig. 3 in the main text).  $\text{Fe}_2\text{TaGa}_{\text{Ge}}$  is in an intermediate case between  $\text{Fe}_2\text{TiSn}_{\text{Sb}}$  and  $\text{Fe}_2\text{NbGa}_{\text{Ge}}$  (not shown). Interestingly, the localization effect and the magnetic phase transitions also appear upon injection of additional electrons in the pristine structures with a compensating positively charged background: this suggests a strictly electronic origin of these phenomena.

### Nature of the donors

We investigated the role of the dopants species by computing the band structure of  $\text{Fe}_2\text{TiSn}$  doped with As instead of Sb, shown in Fig. 12. An exchange splitting of 0.25 eV is witnessed between the minority and majority spin population near the conduction band minimum, similar to what is observed for  $\text{Fe}_2\text{TiSn}_{\text{Sb}}$ . Hence, we do not expect the nature of the donor to play a significant role in the observed magnetic properties. This is further justified in the following Sections.

### Artificial doping within B1-WC

To disentangle the atomic size effect (due to the different size of the dopant with respect to the substituted atom in the pristine phase) from the electron doping itself, the localization of additional carriers is also witnessed in a  $2 \times 2 \times 2$  supercell of  $\text{Fe}_2\text{YZ}$ , by adding a single electron and a compensating charged background at fixed cubic geometry (in a Jellium-like picture), in order to mimic the effect of the  $x = 1/32$  substitution. The corresponding band structures for (a)  $\text{Fe}_2\text{TiSn}$ , (b)

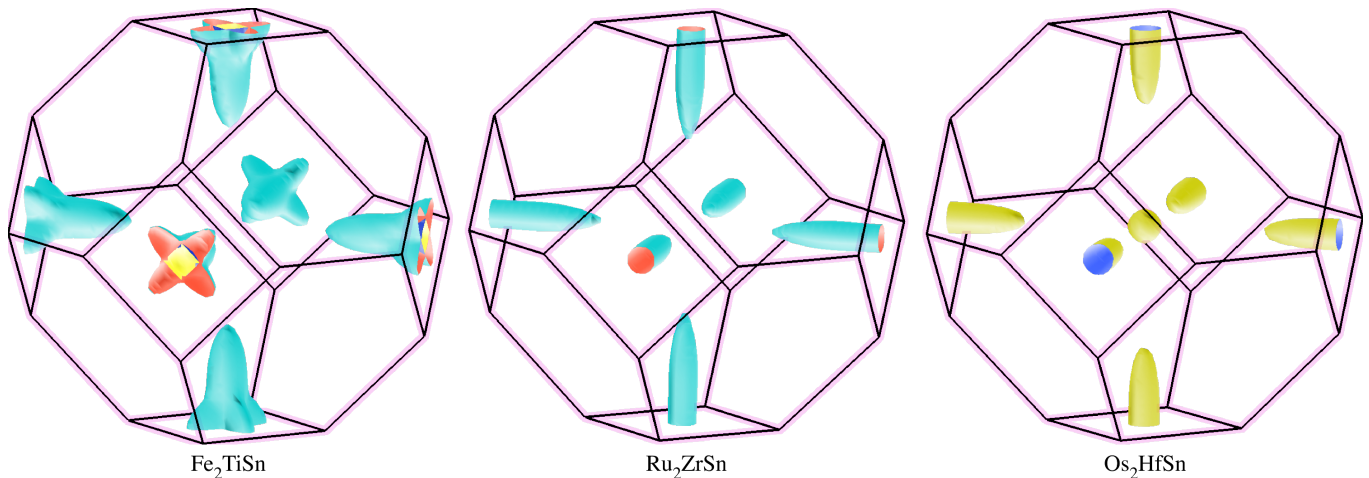


FIG. 9. Fermi Surfaces without SOC interaction, as calculated from GGA+ $U$ .

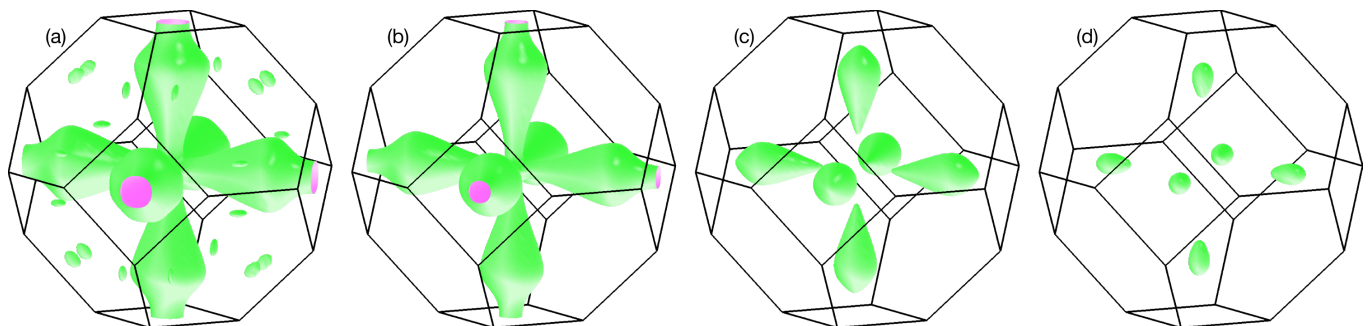


FIG. 10.  $\text{Os}_2\text{HfSn}$  Fermi Surfaces including SOC interaction at: (a) major PF peak; (b) 90% of major PF peak; (c) PF flat region; (d) 90% of PF flat region, as calculated from GGA+ $U$ .

$\text{Fe}_2\text{NbGa}$  and (c)  $\text{Fe}_2\text{VAl}$  are shown in Fig. 13. In the case of  $\text{Fe}_2\text{TiSn}$ ,  $E_F$  is shifted toward the conduction band, and the Fe  $e_g$  states evidence an exchange splitting (200 meV/cell), similarly to the explicitly doped case. On the contrary, no exchange splitting occurs for  $\text{Fe}_2\text{NbGa}$  and  $\text{Fe}_2\text{VAl}$  again in agreement with the explicitly doped procedure. The role of the Y  $e_g$  orbitals is fundamental in this phenomenon: the population belonging to the flat region (Fe  $e_g$ , with high effective mass and low mobility) is expected to localize in real space and its strong electronic exchange interaction favours the spin-splitting, whereas the one on the highly dispersive band (Y  $e_g$ , with low effective mass and high mobility), delocalizes and disadvantages the magnetic phase.

The interplay between magnetization and localization can be studied through the specific case of  $\text{Fe}_2\text{TiSn}$  as illustrated in Fig. 14, where the band structures are plotted for the  $2 \times 2 \times 2$  supercell doped with (a) one electron in its FM ground-state (same Figure as Fig. 13(a)), (b) for the non-magnetic (NM) constrained phase and (c) the pristine phase. The band profile in Fig. 14(b) and Fig. 14(c) cases mostly only differs by the position of the  $E_F$ . This shows that the impurity atom Sb is not even needed for the exchange-splitting to manifest (with a gain of energy of 44 meV with respect to the NM phase), sug-

gesting an electronic origin.

The associated electron densities for the added carriers are shown in Fig. 15(a) for the FM ground state and Fig. 15(b) for the NM constrained phase. In the first case, localization occurs: the pattern of electron density is the same as in the explicitly doped case (Fig. 15(c), while in the second case, the charge is completely delocalized over the Fe, as expected from the rigid band approximation. As a consequence of these results, the localization of carriers strictly shows an electronic origin and is associated with a magnetic instability.

We verified that the electronic nature of the magnetic instability appearing in  $\text{Fe}_2\text{TiSn}$ ,  $\text{Fe}_2\text{TiSi}$  and  $\text{Fe}_2\text{TaGa}$  is Stoner-type [25, 26]. For this purpose, the Stoner criterion is evaluated for all the doped compounds, accounting for the exchange splitting  $\Delta E_{ex}$  and the non-magnetic phase DOS at  $E_F$ ,  $\text{DOS}^{(\text{NM})}(E_F)$ . According to the Stoner model of the ferromagnetism, a magnetic instability occurs when:

$$St = \text{DOS}^{(\text{NM})}(E_F) \cdot \Delta E_{ex} > 1 \quad (5)$$

The results obtained are listed in Tab. III and, very interestingly, each compound showing a FM phase fulfils the criterion. For  $\text{Fe}_2\text{VAl}$  and  $\text{Fe}_2\text{NbGa}$ ,  $St < 1$ , as expected from the DFT results. These results suggest that

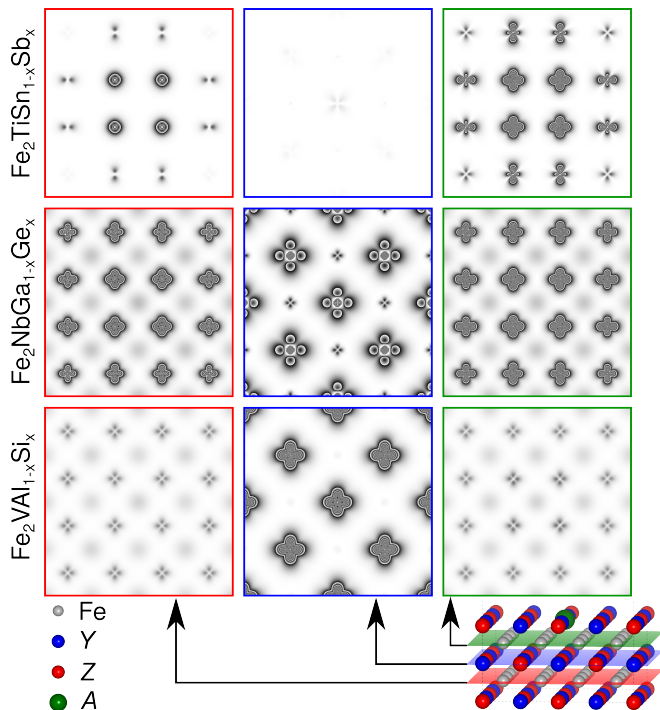


FIG. 11. Electron density of the additional electrons as calculated from B1-WC, at  $x = 1/32$ , computed on the (001) planes at different distances from the origin, corresponding respectively to Fe, X/Y and Fe atomic planes. The latter is the closest Fe (grey spots) plane to the impurity A (green spot). At the bottom, half-cut of the cell is shown with the atoms indicated in the bottom-left legend highlighting with colors (red, blue and green) the planes where the charge density has been projected.

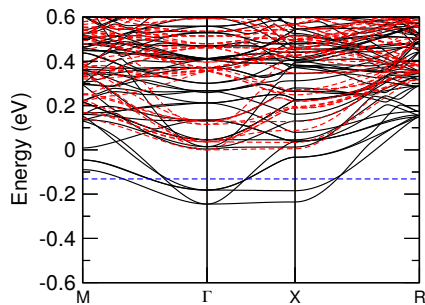


FIG. 12. Spin resolved band structure of  $\text{Fe}_2\text{TiSn}_{\text{As}}$  ( $x = 1/32$ ).

the magnetic phase transition as a function of the doping is due to a Stoner instability in  $\text{Fe}_2\text{TiSn}$ ,  $\text{Fe}_2\text{TiSi}$  and  $\text{Fe}_2\text{TaGa}$ .

#### Artificial doping within GGA+U, origin of magnetization

In Fig. 16, we show the spin-polarized DOS at  $E_F$  and the cell magnetization as a function of the electron

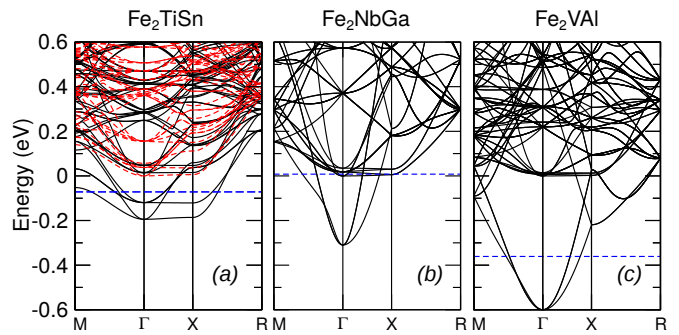


FIG. 13. Ground state band structure of  $\text{Fe}_2\text{YZ}$  computed on  $2 \times 2 \times 2$  supercells (at fixed geometry) injecting one additional electron, as calculated using B1-WC. Dashed line:  $E_F$ ; black-(red-) line: spin-up (spin-down) channel.

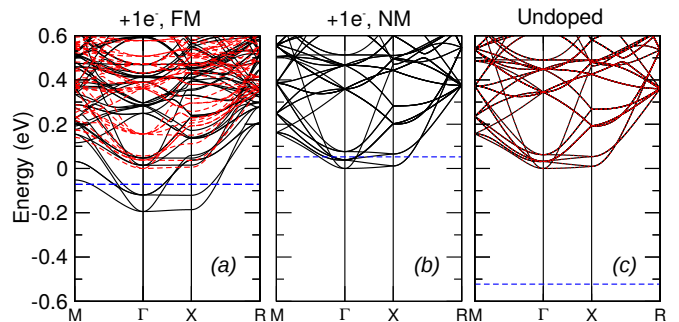


FIG. 14. Band structure of  $\text{Fe}_2\text{TiSn}$  computed on  $2 \times 2 \times 2$  supercell (at fixed geometry), as calculated using B1-WC: (a) doped with one additional electron in its FM ground-state; (b) doped with one additional electron in the NM constrained phase; (c) undoped. Dashed line:  $E_F$ ; black-(red-) line: spin-up (spin-down) channel.

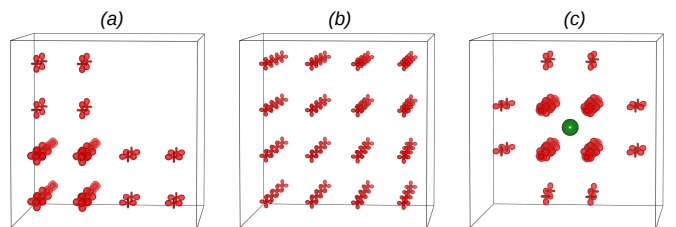


FIG. 15. Isosurfaces of electron density ( $0.004 \text{ Bohr}^{-1}$ ) of the additional carriers in the  $2 \times 2 \times 2$  supercell, as calculated using B1-WC, for: (a) doped with one additional electron in its FM ground state; (b) doped with one additional electron in the NM phase and (c) explicitly doped  $\text{Fe}_2\text{TiSn}_{\text{Sb}}$  at  $x = 1/32$ , the Sb atom is displayed in green.

doping concentration, injected in pristine hosts (without atomic substitution), for the whole series of compounds. As in the main text, we start from the doped  $\text{Fe}_2\text{VAI}$  ((c) panel) which shows a large distance between the two  $e_g$  bands at the X point (larger than the case shown in Fig. 4(a), main text). Here, the additional electrons populate the V  $e_g$  levels at the CBM and, consequently, no spin-splitting is induced up to  $3.0 \times 10^{21} \text{ cm}^{-3}$ , perfectly in agreement with B1-WC explicit doping, and as expected

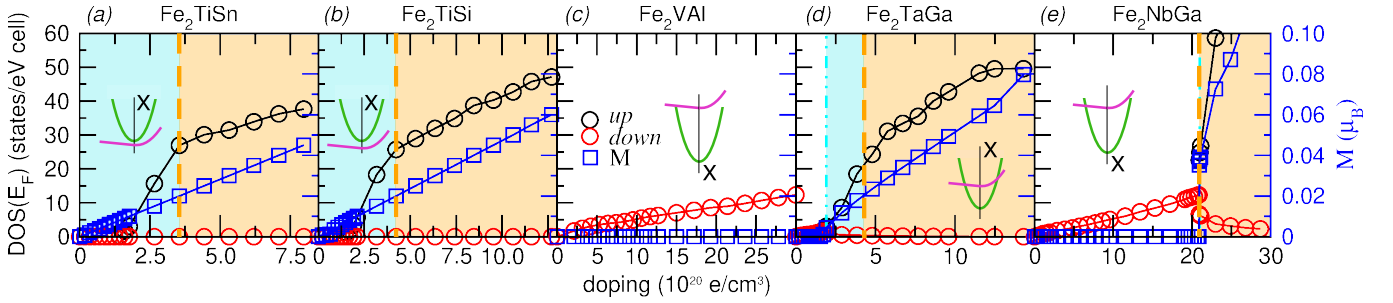


FIG. 16. GGA+ $U$  results: spin-projected DOS at  $E_F$  and cell magnetization versus doping for the five compounds: black (red) open circles refer to up (down) spin channels (left axis), open squares (blue) to the cell magnetization (blue right axis). Cyan double-dot-dashed line: critical carrier concentration needed to begin to populate the Fe  $e_g$  state; orange dashed line: critical doping for which the Stoner criterion is verified ( $St > 1$ ).

$Fe_2YZ$	$\Delta E_{ex}$ (eV)	$g^{NM}(E_F)$ (st./eV)	$St$
$Fe_2TiSn$	0.200	35.31	7.1
$Fe_2TiSi$	0.154	37.84	5.8
$Fe_2VAl$	0.000	8.07	0.0
$Fe_2TaGa$	0.097	25.14	2.4
$Fe_2NbGa$	0.060	13.76	0.8

TABLE III. Evaluation of the Stoner criterion using Eq. (5): exchange splitting  $\Delta E_{ex}$  and the value of the NM phase DOS at  $E_F$   $g^{NM}(E_F)$  calculated using B1-WC.

from fully delocalized states. Increasing the amount of doping more than  $5.7 \times 10^{21} \text{ cm}^{-3}$  the system results unstable (large cell pressures) and its charge density is difficult to converge. In the  $Fe_2NbGa$  (Fig. 16(e)) no spin-polarization manifests while the Nb  $e_g$  band is populated and Fe one remains empty (analogously to Fig. 4(a) and (b), main text). The magnetic transition appears when electrons are allocated on the Fe  $e_g$  band with high local magnetic moments with interaction mediated by the itinerant electrons on the Nb site. Here, in fact, the validity of the Stoner condition ( $St > 1$ , see Eq. (5) and main text) is reached at  $2.1 \times 10^{21} \text{ cm}^{-3}$  (highlighted with orange dashed line).  $Fe_2TaGa$  (Fig. 16(d)), analogously to  $Fe_2VAl$  and  $Fe_2NbGa$ , shows the Ta  $e_g$  state at the CBM. However, differently to those cases, the distance between the two bands is lower resulting in a stronger hybridization (as Fig. 4(c) main text). This particular band relative position has very interesting consequences: the system goes across three main regimes induced by doping: at low concentrations, we start to populate the Ta  $e_g$  level and at about  $1.7 \times 10^{20} \text{ cm}^{-3}$  (maroon dot-dashed line) an exchange splitting is induced on Fe  $e_g$  states although the splitting on the occupied Ta orbitals remains negligible. This behaviour confirms the interplay between orbital hybridization and the exchange interaction: in this region (maroon background, Fig. 16(d)) the direct exchange dominates ( $St < 1$ ): there are not enough delocalized states to favour the itinerant electron

with respect to the direct exchange. For this reason, when the Fe  $e_g$  start to be populated (at critical concentration of about  $1.9 \times 10^{20} \text{ cm}^{-3}$ , starting point of the cyan background region in Fig. 16(d)), its strongly localized nature invalidates even more the itinerant picture ( $St < 1$ ). Increasing the doping density at about  $4.2 \times 10^{20} \text{ cm}^{-3}$  (orange dashed line), a sufficient number delocalized electrons makes the itinerant magnetism dominate and the Stoner condition  $St > 1$  fulfilled. For the last two compounds, we tuned the  $U_{Ti}$  to obtain a similar arrangement of the band structure as obtained with B1-WC, keeping the  $U_{Fe}$  at the self-consistently estimated value.  $Fe_2TiSn$  and  $Fe_2TiSi$  (Fig. 16(a), same as Fig. 4(d) of main text, and (b)), having the Fe  $e_g$  band at the CBM, show an induced spin-polarization and a consequent magnetization immediately (similarly to Fig. 4(d), main text) and in both cases their DOS confirm the acquired half-metallic character. The highly localized nature of the Fe  $e_g$  orbitals and the strong exchange interaction among belonging carriers drive this behaviour. In the low doping region, moreover, the prevalent nature of the exchange interaction, still due to the localized nature of these states, is direct ( $St < 1$ ). However, at about  $3.8 \times 10^{20} \text{ cm}^{-3}$  for  $Fe_2TiSi$  and  $3.6 \times 10^{20} \text{ cm}^{-3}$  for  $Fe_2TiSn$ , the itinerant exchange starts to dominate ( $St > 1$ ) due to the presence of a sufficient number of free-like electrons.

### Thermoelectric properties

In a rigid band picture, doping with donors (acceptors) only shift the chemical potential  $\mu$  from its initial position the gap to bring it closer to the conduction (valence) band. In the case of  $Fe_2YZ$  compounds, given the nature of the band edge (Fe 3d), substitution at the Z site is expected to bring  $\mu$  inside the conduction band, close to the band edge. This effect is highlighted in Fig. 17 for the specific case of  $Fe_2TiSn_{5b}$  at 300 K: the Seebeck coefficient  $S$ , electrical conductivity  $\sigma$ , the correspond-

ing power factor  $S^2\sigma$  as well as the electronic DOS are compared among: the pristine eigen-energies ( $x = 0$ ), the NM phase and the FM phase concentration 1/16. For the explicitly doped case,  $E_F$  lies inside the conduction band, as discussed in the previous section. The calculated values for the transport coefficients are very close to the rigid band predictions in the NM constrained phase; however, for the FM phase (ground-state), the in-gap states reduce the number of carriers (in the  $k_B T$  interval around  $E_F$ ) contributing to  $S$  and  $\sigma$ , with  $\mu$  near the conduction states, resulting in a decrement of the PF peak in the  $n$ -type region. In contrast,  $S$  and  $\sigma$  related a hypotetic  $\mu$  lying in the  $p$ -type region, remain, in both cases, unaffected. We also show the spectral PF of the doped FM phase at 600 K with a corrected relaxation time  $\tau$  to account for phonon scattering at high temperature [1], showing that the peak of power factor remains roughly around  $\sim 3 - 4$  mW/K<sup>2</sup>m at higher temperatures.

- 
- [1] D. I. Bilc, G. Hautier, D. Waroquiers, G.-M. Rignanese, and P. Ghosez, *Physical Review Letters* **114**, 136601 (2015).
- [2] R. Dovesi, R. Orlando, A. Erba, C. M. Zicovich-Wilson, B. Civalleri, S. Casassa, L. Maschio, M. Ferrabone, M. D. L. Pierre, P. D'Arco, et al., *Int. J. Quantum Chem.* **114**, 1284 (2014).
- [3] R. Dovesi, V. R. Saunders, C. Roetti, R. Orlando, C. M. Zicovich-Wilson, F. Pascale, B. Civalleri, K. Doll, N. M. Harrison, I. J. Bush, et al., *CRYSTAL14 User's Manual* (2014).
- [4] D. I. Bilc, R. Orlando, R. Shaltaf, G. M. Rignanese, J. Iniguez, and P. Ghosez, *Physical Review B* **77**, 165107 (2008).
- [5] I. de P. R. Moreira, R. Dovesi, C. Roetti, V. R. Saunders, and R. Orlando, *Phys. Rev. B* **62**, 7816 (2000).
- [6] T. Bredow, P. Heitjans, and M. Wilkening, *Phys. Rev. B* **70**, 115111 (2004).
- [7] M. Towler, *Crystal resources page* (2015), URL <http://www.tcm.phy.cam.ac.uk/~mdt26/>.
- [8] E. Ruiz, M. Lluell, and P. Alemany, *Journal of Solid State Chemistry* **176**, 400 (2003), ISSN 0022-4596, special issue on The Impact of Theoretical Methods on Solid-State Chemistry.
- [9] R. Pandey, M. Causa, N. M. Harrison, and M. Seel, *J. Phys.: Condens. Matter* **8**, 3993 (1996).
- [10] A. R. Porter, M. D. Towler, and R. J. Needs, *Phys. Rev. B* **60**, 13534 (1999).
- [11] H. J. Monkhorst and J. D. Pack, *Phys. Rev. B* **13**, 5188 (1976).
- [12] G. K. Madsen and D. J. Singh, *Computer Physics Communications* **175**, 67 (2006).
- [13] X. Gonze and *et al.*, *Computer Physics Communications* **180**, 2582 (2009).
- [14] J. P. Perdew, K. Burke, and M. Ernzerhof, *Physical Review Letters* **77**, 3865 (1996).
- [15] A. I. Liechtenstein, V. I. Anisimov, and J. Zaanen, *Phys. Rev. B* **52**, R5467?R5470 (1995).

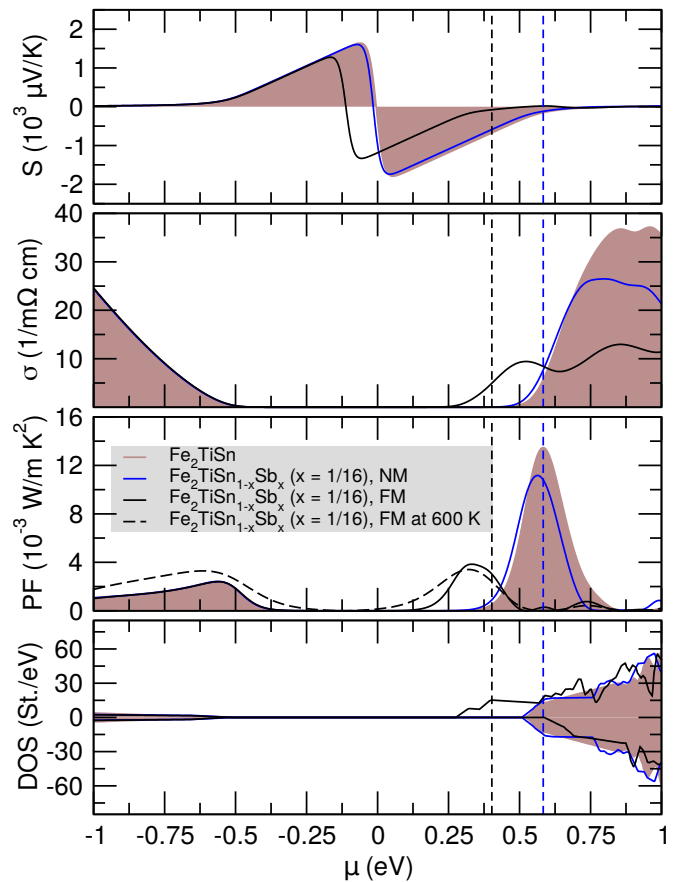


FIG. 17. Room-temperature Seebeck coefficient, electrical conductivity, power factor with respect to chemical potential  $\mu$  of  $\text{Fe}_2\text{TiSn}_{1-x}\text{Sb}_x$  for  $x = 0$  (brown background) and 1/16, NM (blue) and FM (black) magnetic phases. The associated electronic DOS are also given (with positive and negative value for spin-up and spin-down electron respectively). The zero energy is set as  $E_F$  of the pristine material, the vertical dashed lines are the Fermi level  $E_F$  for the doped phases. The transport properties have been computed using the B1-WC band structures.

- [16] M. Cococcioni and S. de Gironcoli, *Phys. Rev. B* **71**, 035105 (2005), URL <https://link.aps.org/doi/10.1103/PhysRevB.71.035105>.
- [17] M. Torrent, F. Jollet, F. Bottin, G. Zérah, and X. Gonze, *Computational Materials Science* **42**, 337 (2008).
- [18] F. Jollet, M. Torrent, and N. Holzwarth, *Comp. Phys. Comm.* **185**, 1246 (2014).
- [19] A. Ślebarski, *Journal of Physics D: Applied Physics* **39**, 856 (2006).
- [20] M. Meinert, M. P. Geisler, J. Schmalhorst, U. Heinzmann, E. Arenholz, W. Hetaba, M. Stöger-Pollach, A. Hütten, and G. Reiss, *Phys. Rev. B* **90**, 085127 (2014).
- [21] Y. Nishino, *Materials Science Forum* **449-452**, 909 (2004).
- [22] A. Baldereschi and R. Resta, eds., *Shallow Impurity Centers in Semiconductors* (Elsevier, Oxford, 1987), ISBN 978-0-444-87087-2, URL <https://www.sciencedirect.com/science/article/pii/B9780444870872500020>.

- [23] J. M. Spaeth and H. Overhof, *Point Defects in Semiconductors and Insulators* (Springer-Verlag Berlin Heidelberg, 2003), ISBN 978-3-319-23879-1.
- [24] M. Grundmann, *The Physics of Semiconductors* (Springer-Verlag Berlin Heidelberg, 2006), ISBN 978-3-540-42695-0.
- [25] E. C. Stoner, Proceedings of the Royal Society of London A: Mathematical, Physical and Engineering Sciences **165**, 372 (1938), ISSN 0080-4630.
- [26] C. M. Teodorescu and G. A. Lungu, Journal of Optoelectronics and Advanced Materials **10**, 3058 (2008).